Energy Conversion and Management 50 (2009) 1722–1729

Contents lists available at ScienceDirect

Energy Conversion and Management

journal homepage: www.elsevier.com/locate/enconman

High-performance sensorless nonlinear power control of a flywheel energy storage system

S.J. Amodeo *, H.G. Chiacchiarini, J.A. Solsona, C.A. Busada

Departamento de Ingeniería Eléctrica y de Computadoras, Instituto de Investigaciones en Ingeniería Eléctrica "Alfredo Desages",
Universidad Nacional del Sur y CONICET, Avda. Alem 1253, (B8000CPB) Baháa Blanca, Argentina

ARTICLE INFO

Article history:
Received 9 August 2008
Accepted 14 March 2009
Available online 18 April 2009

Keywords:
Flywheels energy storage systems
Homopolar synchronous machine
Luenberger observer
Sensorless
Feedback linearization

ABSTRACT

The flywheel energy storage systems (FESS) can be used to store and release energy in high power pulsed systems. Based on the use of a homopolar synchronous machine in a FESS, a high performance model-based power flow control law is developed using the feedback linearization methodology. This law is based on the voltage space vector reference frame machine model. To reduce the magnetic losses, a pulse amplitude modulation driver for the armature is more adequate. The restrictions in amplitude and phase imposed by the driver are also included. A full order Luenberger observer for the torque angle and rotor speed is developed to implement a sensorless control strategy. Simulation results are presented to illustrate the performance.

1. Introduction

Nowadays, energy storage systems are being considered to improve the efficiency of the operation of many systems. Particularly, their inclusion in power system networks improves the system stability by managing faster load fluctuations and complementing the currently growing dispersed generation. This scheme allows the traditional non-renewable generation to operate by supplying low frequency components of the load changes, hence that they can be dispatched in more efficient operation points to achieve an optimization of the natural resources consumption [7,1].

In this field, the energy storage system based on flywheels (FW) is an old technology that is reappearing [4,6], mainly due to the advantages of new developments in composite materials and power electronic devices and to the increasing demand on power quality improvement.

The energy is stored in kinetic energy form, which is proportional to the rotor inertia and the square of the rotational speed. The high composite material strength allows the continuous increase of the admissible rotation speeds (e.g. up to 50–100.000 rpm [5,6]) and consequently, of the energy storage density. These systems present advantages when they are used for supplying pulsed loads or in cases where high power is transferred to/from the system [10–12]. Main advantages of FW are high energy density, long life, the ability to perform deep discharges without component degradation [4] and others. They are composed of an electrical machine (motor/generator) connected to an inertial storage device by a mechanical link [10,5], or in some cases the rotor of the electrical machine is the storage element itself [15,14].

The electrical machine, necessary to produce the electromechanical conversion, accelerates the storage device to collect incoming power and decelerates it for releasing power. Long-term storage can be obtained by reducing the mechanical losses by means of enclosing the rotating parts in a moderate vacuum and using magnetic bearings [8]. This restricts the possibility of heat dissipation only by radiation, so the heat losses in the rotor are critical.

Several kinds of machines are used in FW systems. The most common types are Permanent Magnet Synchronous Machines (PMSM) [13], Induction Machines (IM) [16,4] and Homopolar Synchronous Machines (HSM) [15,14]. The HSM has a robust rotor, which can be constructed out of a one-piece solid ferromagnetic material. The absence of the field winding in the rotor provides low rotor losses and enhances mechanical reliability. For these reasons and its high efficiency the HSM results a very suitable machine for the FW application. Since the FW operates at high frequency and power, a pulse width modulation (PWM) strategy is not suitable, as it would need to operate the drive at extremely high switching frequency, producing high driver losses and also increasing critical rotor losses considerably. Therefore, a pulse amplitude modulation technique (PAM) is a more appropriate modulation strategy [17]. This fact restricts the locus of the space vectors that could be applied to the armature just to discrete

---

* Corresponding author.
E-mail addresses: samodeo@uns.edu.ar, santiago.amodeo@gmail.com (S.J. Amodeo).

0196-8904/$ - see front matter © 2009 Elsevier Ltd. All rights reserved.
doi:10.1016/j.enconman.2009.03.024

positions with constant magnitude (six active space vectors for a three-phase machine).

Even more, to further reduce the harmonics core losses it is necessary to reduce the level of the lower harmonic components of the input waveforms while preserving the fundamental frequency component. This can be achieved by using a more sophisticated multilevel driver for the same three-phase machine, or using a polyphase machine. The selection of the best configuration is outside the scope of the present work, although for this case, a HSM with dual three-phase asymmetrical ($D-3\phi$) armature windings driven by three-phase multilevel inverters ($3\phi MI$) [9] is used. This configuration operating with adequate PAM produces 12 active vector equally spaced $\pi/6$ rad in $\alpha\beta$ plane. This modulation should also reduce the circulating harmonics induced in $x-y$ zero sequence components [2,3]. The benefits of this scheme are that it reduces flux ripple and magnetic losses, and produces power segmentation. The field voltage is synthesized with a PWM DC–DC converter connected to the constant DC-link of the system. Fig. 1 shows a simplified scheme of the whole system.

The control objective is to manage the bidirectional power flow towards the HSM based FW (see Fig. 1). A sensorless control strategy of this system based on linear controllers was presented in [18]. One of its main advantages, as mentioned in that work, is the simplicity of the control, because an observer for the mechanical states is not necessary. However, due to the strong coupling between the control loops, the transient and stationary performances are limited. Here it is proposed a high-performance sensorless control that uses a load angle observer that could be able to be implemented without major hardware modifications or cost increase.

This work continues the presented in [19], where two high-performance control strategies were proposed. Because of its better reactive power regulation, here it is used the control strategy based on the HSM model expressed on a rotating reference frame attached to the stator voltage space vector (denominated *DQf* in that work). In the present work it is incorporated an observer for the mechanical variables to implement the control strategy without mechanical sensors (sensorless). This is an important issue for this application because the high velocity rotation of the rotor makes the mechanical measurements troublesome. The control strategy for the HSM is based on feedback linearization [20]. This control technique has been widely used elsewhere to regulate mechanical variables on different kinds of electrical machines [21,22]. In [13] a control strategy with feedfoward decoupling for a PMSM FW is used.

This paper is organized as follows. Section 2 includes a brief description of the HSM and its mathematical model, including its representation on a rotating frame attached to the stator voltage space vector. Section 3 presents the control strategy, including the observer. Section 4 shows simulation results, first on the assumption that there is no saturation of the manipulated variables and nominal plant case. Then the control performance is analyzed under parametric uncertainty, later incorporating the actuator phase restriction. Finally, Section 5 presents the conclusions and future work.

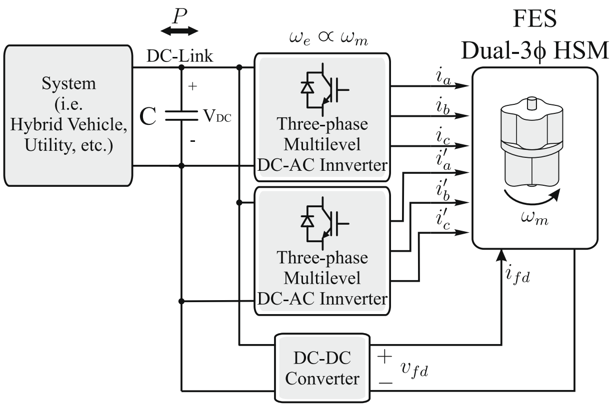

Fig. 1. Schematic diagram of the system.

2. $D-3\phi$ homopolar synchronous machine

This machine operates under similar principles than the standard synchronous machine. Both have identical terminal connections. However, the HSM has the field winding mounted in the stator around the rotor. Therefore, the field flux flows axially in the center part of rotor and then an adequate rotor profile orientates the flux radially, so it is produced the induction as in traditional synchronous machines. The rotor is solid and made from a unique piece of material. More details can be found in [14] where an experimental prototype is included. This machine is not widely used since the flux path is longer than in standard SM, so it is necessary a higher mmf (and consequently, higher energy) for its magnetization. On the contrary it has the advantage of having lower rotor losses and does not use slip rings for connecting the field winding.

2.1. Model in $\alpha-\beta$ coordinates

Using the following decoupling transformation (Clarke), the original phase electromagnetic variables are transformed into a new set of six variables in a orthogonal basis [3].

$$\begin{bmatrix} S_\alpha \\ S_\beta \\ S_x \\ S_y \\ S_{0^+} \\ S_{0^-} \end{bmatrix} = \frac{1}{\sqrt{3}} \begin{bmatrix} 1 & -\frac{1}{2} & -\frac{1}{2} & \frac{\sqrt{3}}{2} & -\frac{\sqrt{3}}{2} & 0 \\ 0 & \frac{\sqrt{3}}{2} & -\frac{\sqrt{3}}{2} & \frac{1}{2} & \frac{1}{2} & -1 \\ 1 & -\frac{1}{2} & -\frac{1}{2} & -\frac{\sqrt{3}}{2} & \frac{\sqrt{3}}{2} & 0 \\ 0 & -\frac{\sqrt{3}}{2} & \frac{\sqrt{3}}{2} & \frac{1}{2} & \frac{1}{2} & -1 \\ 1 & 1 & 1 & 0 & 0 & 0 \\ 0 & 0 & 0 & 1 & 1 & 1 \end{bmatrix} \begin{bmatrix} S_a \\ S_b \\ S_c \\ S_{a'} \\ S_{b'} \\ S_{c'} \end{bmatrix}, \tag{1}$$

where S_i represents an electromagnetic variable (i.e. currents, voltages, flux, etc.). The first two rows in (1) are the $\alpha-\beta$ components which are the only ones where stator to rotor coupling appears. So, they are the only components associated with torque production. The last two rows are associated to the zero sequence components. The machine is star connected without neutral conductors, so the applied zero sequences components are eliminated. The other two components, called $x-y$, are completely decoupled without stator to rotor coupling. As well, these components do not contribute to torque production. The stator leakage impedance and the windings resistances are the only impedances of the machine to the useless $x-y$ currents circulation. This issue is of particularly importance when implementing the PAM strategy with a specific multilevel technique designed for minimizing the currents produced by the $x-y$ components.

As stator to rotor coupling takes place only in the $\alpha-\beta$ plane the model is only developed in these axes. In a stationary $\alpha-\beta$ reference frame the flux equations are

$$\boldsymbol{\lambda}_{\alpha\beta f} = \mathbf{L}_{\alpha\beta f}\mathbf{i}_{\alpha\beta f}, \tag{2}$$

where

$$\mathbf{L}_{\alpha\beta f} = \begin{bmatrix} L & 0 & L_m\cos(P\theta_m) \\ 0 & L & L_m\sin(P\theta_m) \\ L_m\cos(P\theta_m) & L_m\sin(P\theta_m) & L_{fd} \end{bmatrix},$$

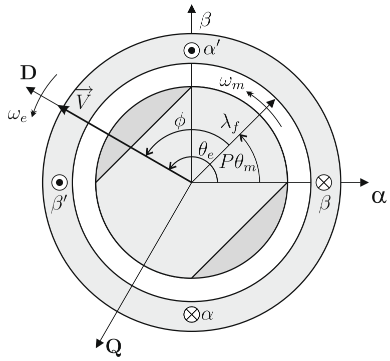

Fig. 2. Voltage *DQf* and stationary $\alpha\beta$ references frames.

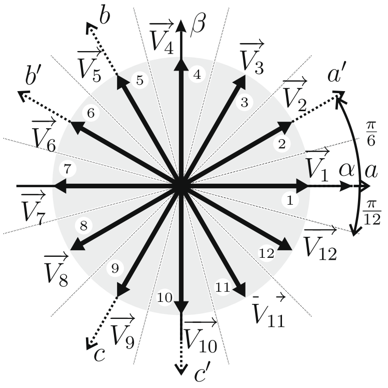

Fig. 3. Active voltage space vectors.

is the inductance matrix; L, L_{fd} and L_m are the armature, field and mutual inductance, respectively; P is the number of pole-pairs and θ_m is the rotor position. The two-axis equivalent model results

$$\dot{\boldsymbol{\lambda}}_{\alpha\beta f} = -\mathbf{R}\mathbf{L}_{\alpha\beta f}^{-1}\boldsymbol{\lambda}_{\alpha\beta f} + \mathbf{v}_{\alpha\beta f}, \tag{3}$$

where $\mathbf{R} = Diag\{R, R, R_{fd}\}$ is the resistance matrix; R and R_{fd} are the armature and field resistances and $\mathbf{v}_{\alpha\beta f}$ is the $\alpha\beta$ components and field applied voltages vector. The currents state model is obtained differentiating (2) as

$$\dot{\mathbf{i}}_{\alpha\beta f} = \mathbf{P}_{\alpha\beta f}\mathbf{i}_{\alpha\beta f} + \mathbf{L}_{\alpha\beta f}^{-1}\mathbf{v}_{\alpha\beta f}, \tag{4}$$

where

$$\mathbf{P}_{\alpha\beta f} = -\mathbf{L}_{\alpha\beta f}^{-1}\mathbf{R} + \dot{\mathbf{L}}_{\alpha\beta f}^{-1}\mathbf{L}_{\alpha\beta f} \tag{5}$$

and

$$\dot{\mathbf{L}}_{\alpha\beta f}^{-1} = d\mathbf{L}_{\alpha\beta f}^{-1}/dt = \omega_m d\mathbf{L}_{\alpha\beta f}^{-1}/d\theta_m. \tag{6}$$

The torque expression is

$$\tau_e = L_m P i_{fd}(i_\alpha \sin(P\theta_m) - i_\beta \cos(P\theta_m)). \tag{7}$$

No external perturbation torque is applied to the rotor because it has not any mechanical links with other devices. Therefore, the mechanical frequency of the rotor is governed by

$$\dot{\omega}_m = \frac{1}{J}(\tau_e - B\omega_m), \tag{8}$$

and the angular position is $\dot{\theta}_m = \omega_m$.

2.2. Reference frame transformations

It is convenient to express the model equations in a rotating synchronous coordinate frame. The coordinate transformation from the $\alpha\beta f$ frame to this new rotating frame is

$$\mathbf{T} = \begin{bmatrix} \cos(\gamma) & \sin(\gamma) & 0 \\ -\sin(\gamma) & \cos(\gamma) & 0 \\ 0 & 0 & 1 \end{bmatrix}, \tag{9}$$

where γ is the angular position of the direct axis on the new reference frame. We called *DQf* the reference frame that defines its direct axis D aligned with the spatial voltage vector applied by the driver ($\gamma = \theta_e$) and the associated transformation is called $\mathbf{T}_{DQf} = \mathbf{T}|_{\gamma=\theta_e}$. Fig. 2 shows the position of this reference frame.

2.2.1. HSM model in DQf coordinates

Transforming the electrical variables using $\mathbf{T}_{DQf}$ the model becomes

$$\dot{\mathbf{i}}_{DQf} = \mathbf{Q}_{DQf}\mathbf{i}_{DQf} + \mathbf{L}_{DQf}^{-1}\mathbf{v}_{DQf}, \tag{10}$$

where

$$\mathbf{Q}_{DQf} = \dot{\mathbf{T}}_{DQf}\mathbf{T}_{DQf}^{-1} + \mathbf{T}_{DQf}\mathbf{P}_{\alpha\beta f}\mathbf{T}_{DQf}^{-1} \tag{11}$$

and

$$\mathbf{L}_{DQf} = \mathbf{T}_{DQf}\mathbf{L}_{\alpha\beta f}\mathbf{T}_{DQf}^{-1}. \tag{12}$$

Since the axis D in the *DQf* frame is aligned with the armature voltage spatial vector, the voltage vector in *DQf* coordinates results $\mathbf{v}_{DQf} = [U_A \quad 0 \quad v_{fd}]^T$, where U_A is the amplitude of the applied spatial vector.

In this formulation an extra state equation appears explicitly. Differentiating $\phi := \theta_e - P\theta_m$, it results:

$$\dot{\phi} = \omega_e - P\omega_m. \tag{13}$$

The electromagnetic torque, expressed in terms of currents respect of the coordinates *DQf* becomes

$$\tau_e = L_m P i_{fd}(i_Q \cos(\phi) + i_D \sin(\phi)). \tag{14}$$

Then, the model of the HSM in coordinates *DQf* is defined by Eqs. (10), (13) and (8). The inputs are the amplitude U_A of the voltage spatial vector, its electrical frequency ω_e and the voltage applied to the field winding v_{fd}.

2.2.2. Active space vectors

Since the inverters operate at a constant DC-link voltage, and it is not desirable to perform a PWM strategy, an additional restriction to the model appears. This restriction limits the possibility to produce active voltage vectors of only constant amplitude and discrete phase angles. The twelve 30° equally spaced active vectors obtained from the scheme of the machine and the drives adopted are indicated in Fig. 3. This amplitude restriction results in $U_A = U$, where U is the constant amplitude of the space vectors for the model in *DQf* coordinates. Due to this restriction the HSM model manipulated variables are reduced to ω_e and v_{fd}.

3. Control strategy

Since the FW is used for energy storage, it is desirable to control the bidirectional electric power flow of the machine. The rotation speed is maintained between operating limits, and regulated at its optimal value (depending on the application) by means of an external control loop which is not included in this paper.

The control strategy developed here only considers the amplitude restriction mentioned in the previous section. The discrete angular magnitude will produce a perturbation, which will be filtered out with an adequate sampling, that will be analyzed later by simulation. The constant amplitude U of the applied voltage space vector corresponds to the fundamental component of the PAM adopted. Measurements of the armature and field currents are supposed to be available for the controller.

3.1. DQf control strategy

In this reference frame the current component i_D is the only one associated with the active power. To set unity power factor, the component i_Q should be regulated to zero. Then the reference values for each component are

$$i_D^{\star} = P^{\star}/U, \quad i_Q^{\star} = 0, \tag{15}$$

where $P^{\star}$ is the active power reference.

As stated before, when the voltage amplitude restriction (due to the drive) is included, the system inputs are reduced to ω_e and v_{fd}. It was found that the linearization scheme leads to stable zero dynamics only if the states i_Q from (10) and ϕ are chosen for linearization. Replacing in (10) with the following control law:

$$\begin{aligned}
v_{fd} = {} & \frac{1}{L_m L}(i_{fd}LL_mR_{fd} + L_m^2(-i_DR + U + i_QLP\omega_m)\cos\phi \\
& + \left(L_{fd}L - L_m^2\right)(i_QR + L(v_1 + i_Dv_2 + i_DP\omega_m) \\
& + i_{fd}L_mP\omega_m\cos(\phi))\csc(\phi) + L_m^2(i_QR + i_DLP\omega_m)\sin(\phi)), \\
\omega_e = {} & v_2 + P\omega_m,
\end{aligned} \tag{16}$$

it is obtained

$$\begin{aligned}
\dot{i}_D = {} & \frac{1}{L}(-i_DR + U + i_QL(v_2 + P\omega_m) \\
& - (i_QR + L(v_1 + i_Dv_2 + i_DP\omega_m))\cot(\phi) - i_{fd}L_mP\omega_m\csc(\phi)),
\end{aligned} \tag{17}$$

$$\dot{i}_Q = v_1, \tag{18}$$

$$\dot{\phi} = v_2. \tag{19}$$

The following PI controllers are proposed for regulating i_Q and ϕ at their reference values $i_Q^{\star}$ and $\phi^{\star}$:

$$v_1 = k_p^Q(i_Q^{\star} - i_Q) + k_i^Q\int\left(i_Q^{\star} - i_Q\right)dt, \tag{20}$$

$$v_2 = k_p^{\phi}(\phi^{\star} - \phi) + k_i^{\phi}\int(\phi^{\star} - \phi)dt, \tag{21}$$

where the reference value $\phi^{\star}$ is obtained from

$$\phi^{\star} = k_p^D\left(i_D^{\star} - i_D\right) + k_i^D\int\left(i_D^{\star} - i_D\right)dt, \tag{22}$$

where k_p^x and k_i^x are the proportional and integral gains associated with the variable x, being this one any of the variables i_D, i_Q or ϕ. Then, using a cascaded closed loop controller guaranteeing a fast dynamics for the inner loop that regulates ϕ to its reference value $\phi^{\star}$, it is possible to control i_D at its reference value given by (15). Also, using an uncoupled control loop, the component i_Q is regulated to its reference, so a null reactive could be kept.

Fig. 4 shows the schematic block diagram of the proposed strategy, this diagram will be described in more detail in the Section 4. To implement the transformation (9) it is necessary to use the angle θ_e, given by the driver. The angle ϕ and the angular velocity ω_m are needed but not measurables, so they are obtained using the observer which is described in the next section.

3.2. Observer for ϕ and ω_m

The feedback states transformation and the inner loop of the cascade active power control developed in the previous section use the values of the speed (ω_m) and the torque angle (ϕ). To estimate these values a nonlinear Luenberger observer is implemented. The HSM model used to construct the observer is the *DQf* model presented in the previous section but leaving $\dot{i}_{fd}$ implicitly. This derivative can be considered as a known input which will be obtained filtering the field current measurement. Because the angle of the *DQ* reference frame is generated by the AC drive and therefore known, the currents i_D and i_Q are known as well. So the model results less complex than the one used in the control design and one order reduced. This system can be written as follows:

$$\begin{aligned}
\dot{i}_D &= L^{-1}\left(-i_DR + i_QL\omega_e - \dot{i}_{fd}L_m\cos(\phi) - L_mP\omega_mi_{fd}\sin(\phi) + U\right), \\
\dot{i}_Q &= L^{-1}\left(-i_QR - i_DL\omega_e + \dot{i}_{fd}L_m\sin(\phi) - L_mP\omega_mi_{fd}\cos(\phi)\right), \\
\dot{\omega}_m &= J^{-1}(i_{fd}L_mP(i_Q\cos(\phi) + i_D\sin(\phi)) - B\omega_m), \\
\dot{\phi} &= \omega_e - P\omega_m.
\end{aligned} \tag{23}$$

The output variables are $y = [i_D \quad i_Q]^T$. Defining the auxiliary variable $Z = [e_D \quad e_Q \quad z_3 \quad z_4]^T$, it is proposed the following state transformation:

$$Z = \begin{bmatrix} -L_mP\omega_mi_{fd}\sin(\phi) - \dot{i}_{fd}L^{-1}L_m\cos(\phi) \\ -L_mP\omega_mi_{fd}\cos(\phi) + \dot{i}_{fd}L^{-1}L_m\sin(\phi) \\ i_D \\ i_Q \end{bmatrix} \tag{24}$$

and define this auxiliary variables

$$u = \begin{bmatrix} u_1 \\ u_2 \end{bmatrix} = \begin{bmatrix} Li_Q\omega_e + U \\ -i_D\omega_e \end{bmatrix} \tag{25}$$

Then the resultant system in the new variables is observable and has the following expression:

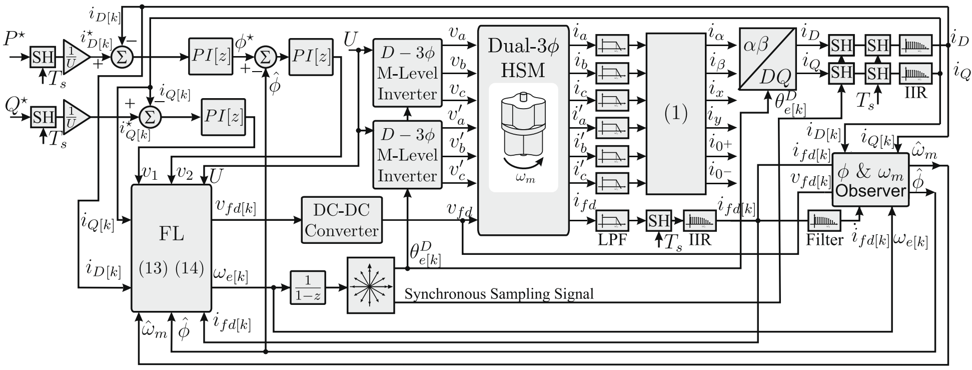

Fig. 4. Control strategy block diagram.

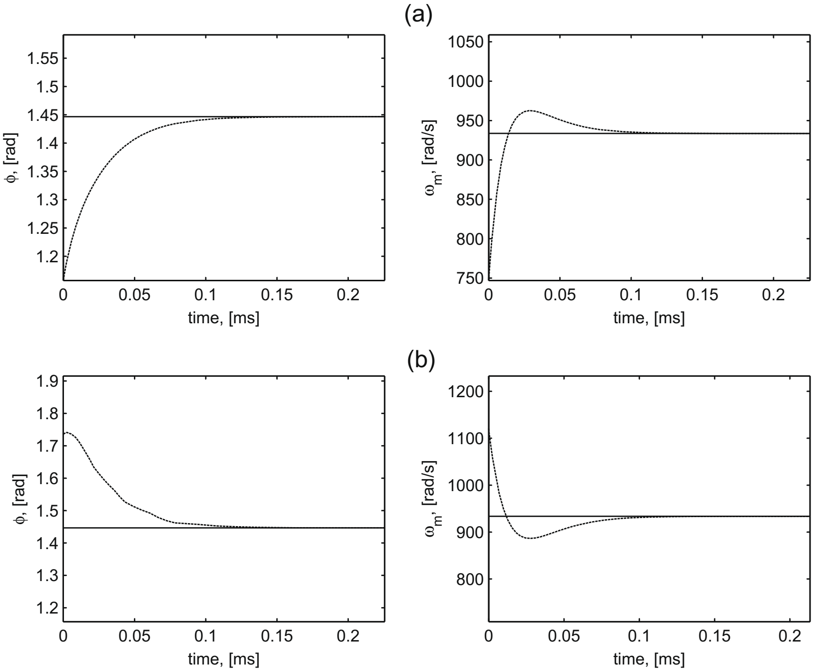

Fig. 5. ϕ and ω observer convergency with an -30% and +30% error in the initial condition, (a) and (b), respectively. Estimated (dashed) and real (continuous) values.

$$\dot{Z} = AZ + \rho(Z) + Bu,$$
$$y = CZ, \tag{26}$$

where

$$A = \begin{bmatrix} -\frac{B}{J} & 0 & 0 & 0 \\ 0 & -\frac{B}{J} & 0 & 0 \\ 1 & 0 & -\frac{R}{L} & 0 \\ 0 & 1 & 0 & -\frac{R}{L} \end{bmatrix}, \quad B = \begin{bmatrix} L^{-1} & 0 \\ 0 & L^{-1} \\ 0 & 0 \\ 0 & 0 \end{bmatrix}, \quad C = \begin{bmatrix} 0 & 0 & 1 & 0 \\ 0 & 0 & 0 & 1 \end{bmatrix}$$

and $\rho(Z)$ has a continuous an bounded Jacobian with respect to Z which satisfies the Lipschitz condition for some bounded constant. Now, the following observer could be built for the system (26) (see [23] for guidelines):

$$\dot{\hat{Z}} = A\hat{Z} + \rho(Z) + Bu + G(y - \hat{y}), \tag{27}$$
$$y = C\hat{Z}. \tag{28}$$

Transforming the estimated states to original variables, $\hat{X} = \begin{bmatrix} \hat{i}_D & \hat{i}_Q & \hat{\omega}_m & \hat{\phi} \end{bmatrix}^T$, the observer equation becomes

$$\dot{\hat{X}} = \hat{M}(\hat{X}) + \Gamma(\hat{X})G\begin{bmatrix} i_D - \hat{i}_D \\ i_Q - \hat{i}_Q \end{bmatrix}, \tag{29}$$

where G is the observer gain matrix and $\hat{M}$ and Γ are the system (23) and the inverse of the jacobian matrix of the state transformation (24) evaluated at the estimated variables. The latest matrix becomes singular if the rotation speed or the field current are zero but these conditions are outside the range where the control strategy will be applied. The gain matrix G must be calculated making a trade off between the desired performance and the measurement noise. Simulation of the observer convergence with positive (+20%) and negatives (-20%) errors in the initial condition of ϕ and ω_m are presented in Fig. 5. The observer asymptotically converged to the real values of ω_m and ϕ.

4. Simulation results

Generally, an operational speed range of the FW from one half to the maximum speed is adopted [14,6]. Since the proposed controller will only be used within the nominal speed range, it is supposed that the FW reaches its minimum speed with another control scheme and then the controller is switched on the fly to the one proposed here. In view of that, the following simulations were done with an error in the initial condition of the states compatible with the one expected at these transitions and supposing that the observer has already converged. The performance of the control strategy is analyzed by simulation using commercial software. The parameters of the machines are listed in Table 1, these correspond to the HSM published in [14]. Three different test condition runs were made. The first one was simulated in continuous time and corresponds to the case of nominal plant, i.e. the controller parameters correspond exactly with the ones of the HSM. Then, results under parametric uncertainties (PU) in continuous time were analyzed. Lately, the results for a discrete time version incorporating the phase restriction of the PAM and also considering PU are presented. The parameters of the controllers were designed as a compromise between the desired dynamic performance and the input exigencies using standard techniques for the nominal plant case. These values were relaxed lately for the non-ideal cases in order to not compromise the system stability. To be able to compare

Table 1
HSM and drive parameters.

Parameter	Unit	Value
P	Pole-pairs	4
J	kg m^2	0.0133
B	μkg m^2/s	24.86
L	μH	33
L_m	mH	1.1
R	Ω	0.1
L_{fd}	mH	257
R_{fd}	Ω	3.44
U	V	70

the effect of these non-idealities, all these tests were made for the same power reference trajectories. The active power reference is a smooth trajectory between −2.8 kW and 2.8 kW. To operate with unity power factor the reactive power reference is kept at zero value.

4.1. Continuous time – nominal plant case

The active power tracking and reactive power regulation results for the nominal plant case are shown in Fig. 6. The correspondent control inputs are shown in Fig. 7 and the estimated values are shown in Fig. 8. For this ideal case it is clear the outstanding performance, the estimated values track the real ones with minimal error and also both power control loops are behaving uncoupled.

4.2. Continuous time – with PU

Simulation results with a mismatch of a 15% in all the inductances and 5% in all the resistances parameters of the controller is performed. The control objective is also attained with a little er-

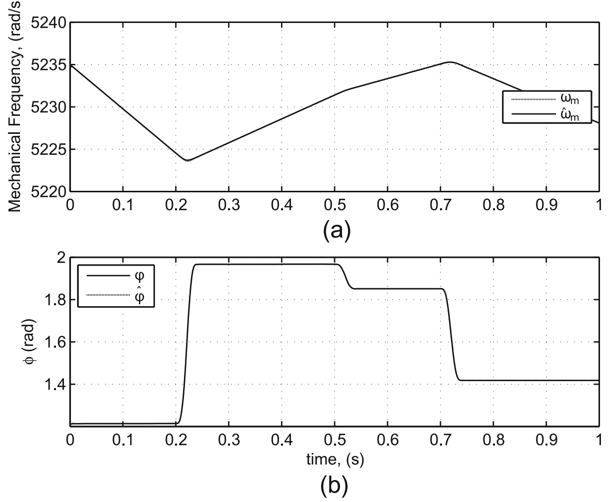

Fig. 8. Nominal case simulation results. Plots (a) and (b) show the real and estimated values of ω_m and ϕ.

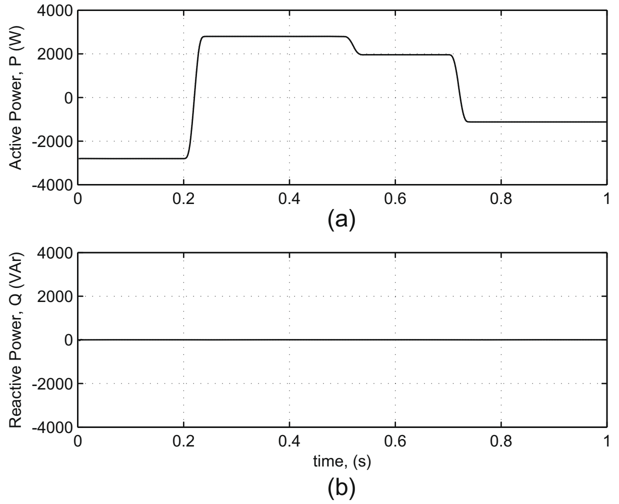

Fig. 6. Nominal case simulation results of a FW pulse charging/discharging, reference trajectory (dashed) and output (continuous). Plots (a) and (b) show the active and reactive power response.

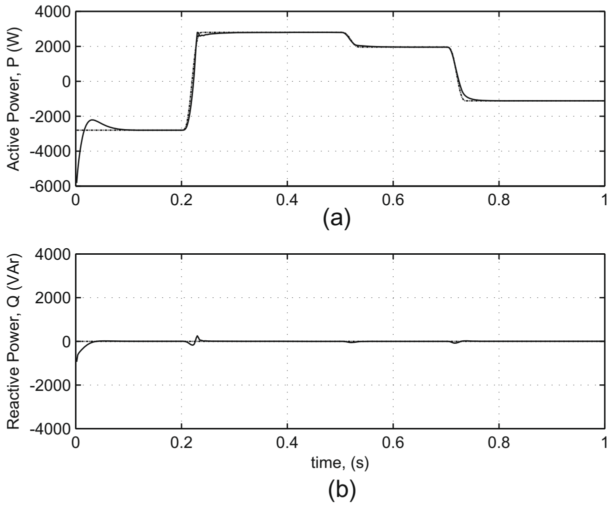

Fig. 9. Parametric uncertain simulation results of a FW pulse charging/discharging, reference trajectory (dashed) and output (continuos). Plots (a) and (b) show the active and reactive power response.

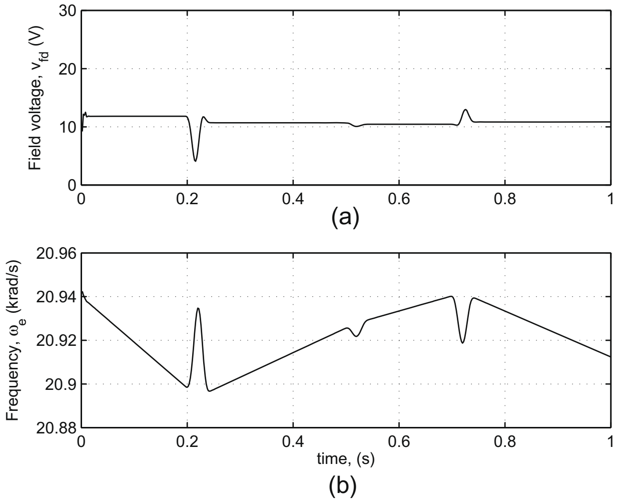

Fig. 7. Nominal case simulation results. Plots (a) and (b) show the control actions ω_e and v_{fd}.

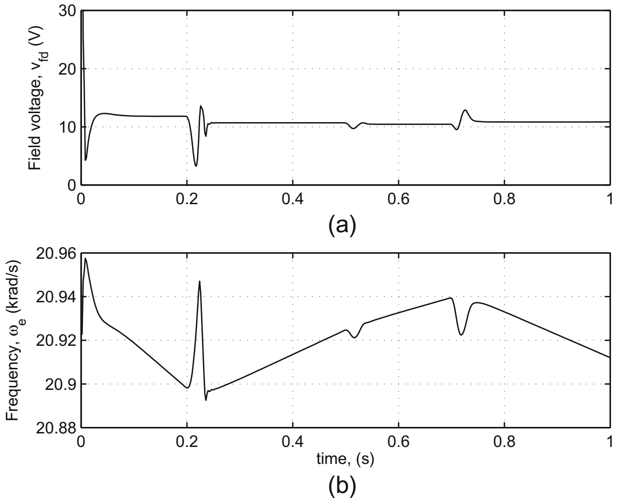

Fig. 10. Parametric uncertain simulation. Plots (a) and (b) show the control actions ω_e and v_{fd}.

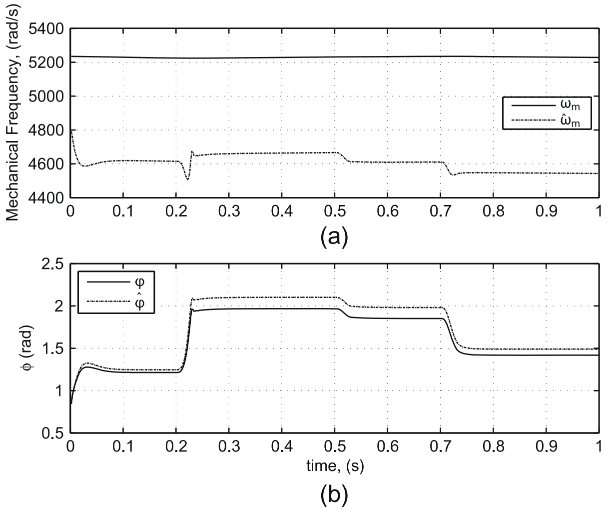

Fig. 11. Parametric uncertain simulation. Plots (a) and (b) show the real and estimated values of ω_m and ϕ.

ror during transients in power reference changes, Fig. 9. In order to cancel the uncertainties, the actuators are more demanded as is shown in Fig. 10. As are shown in Fig. 11, the estimated values have a considerable error. But, up to this uncertainties level, this fact does not compromise the stability of the control.

4.3. Discrete time – with PU and PAM

The PAM is introduced to the model restricting the phase of the applied space vectors (θ_e) only to one of the 12 active space vectors indicated in Fig. 3. Until now the continuous time control considered only the amplitude restriction due to the drives modulation, so was possible to apply any value of θ_e. Now, each space vector has an associated sector of the $\alpha\beta$ plane, as is shown in Fig. 3. So, meanwhile the θ_e produced by the control is within any sector the drive applies the discrete θ_e^D of the sector-associated space vector. The value of U for this simulation was corrected so that the fundamental component of the output waveform has the same amplitude as the one that it would be obtained without the phase discretization.

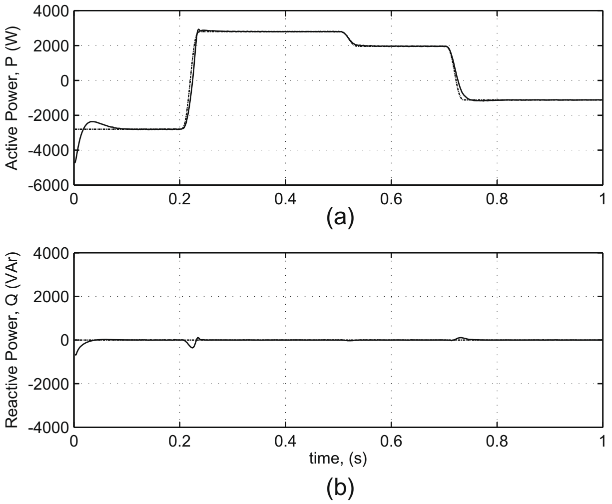

Fig. 12. Parametric uncertainties and PAM simulation results, reference trajectory (dashed) and output (continuos). Plots (a) and (b) show the active and reactive power response.

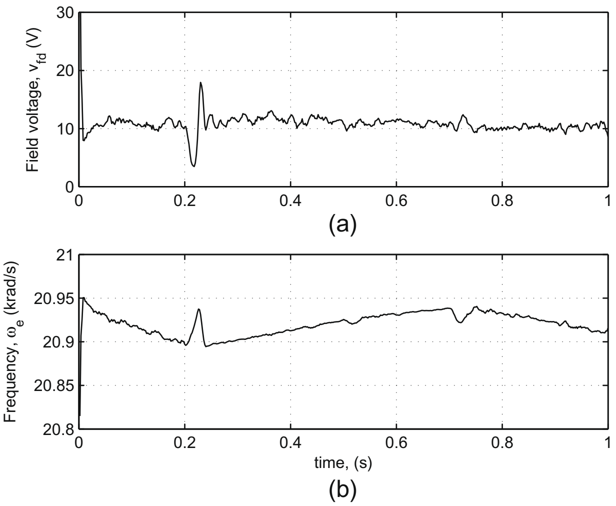

Fig. 13. Parametric uncertainties and PAM simulation results. Plots (a) and (b) show the control actions ω_e and v_{fd}.

To minimize the ripple perturbation introduced by the PAM, a drive-commutation synchronous currents sampling is used. This variable frequency sampling is resampled later at a fixed sample time (T_s). All the previous linear PI controller are discretizated for this sampling. This scheme is detailed in Fig. 4, were the anti-aliasing filters, coordinates transformation and digital filter used are indicated. Also, low pass infinite impulse response digital filters (IIR) are incorporated to attenuate the effects of the current ripple. Filtering the currents in *DQf* coordinates is beneficial because the fundamental components corresponds to DC values, so are easier to filter them. The derivative of the field current necessary for the observer is also obtained using a digital filter.

The results for power tracking in this scheme with the same parametric uncertainties as in the previous section are shown in Fig. 12 and the corresponding manipulated variables in Fig. 13. These results correspond to the sampled and filtered variables. It could be appreciated a low deterioration of the performances of the active power tracking and reactive power regulation but the control objectives are still achieved. The fixed sampling time adopted was 10 μs, so the hardware processor must resolve all the computational operations for the PI controllers and the observer dynamics equations in a shorter time.

5. Conclusions and future work

A sensorless high-performance control strategy for bidirectional power flow on a synchronous homopolar machine working as high-speed flywheel was shown. It was included the voltage restriction imposed by the pulse amplitude modulation drive with a constant DC bus. The variables measured are the stator and field currents. The strategy is based in the application of the vectorial control and feedback linearization to uncouple the currents loops. An almost complete decoupling was obtained with a cascaded control. The case of nominal model was considered and simulation results were shown. In combination with the observer, the strategy showed a fast and adequate dynamic performance during the transient of charge/discharge, and at constant power it perfectly cancels the disturbances due to the velocity changes.

A nonlinear observer for the torque angle and the speed of the rotor, ϕ and ω_m was proposed and used to close the loop of the control strategy. The principal advantage of the *DQf* strategy is that the angle of the reference frame transformation is known, so it is possible to obtain all the electrical states in that coordinated system.

The behavior of the strategy incorporating the phase discretization of the space vector owed to the PAM of the drive was also analized. The disturbance introduced by the modulation was considerably attenuated with an adequate sampling and discrete filter combination. The manipulated variables are considerably demanded. In particular, if the input field voltage v_{fd} waveform had a wide bandwidth with high peaking, it would complicate the design of the driver (DC–DC converter). Due to the required sampling time and the computational cost involved, the required performance for the hardware is very high but could be attainable. In [21] are presented experimental results for a PMSM with similar exigencies for the controller and observer developed.

The simulation results obtained with all the exposed non-idealities and discrete controllers are promissory. At present, a prototype of FESS is under development, which will be used to experiment this control strategy.

Acknowledgements

The present work was partially supported by the PGI 24/K021 (UNS), PGI 24/K033 (UNS), PIP6101 (CONICET, 2004), PICT21811-27 (ANPCYT, 2004), PICTO-UNS814 (ANPCYT, 2004) and PIP 112-200801-02671 (CONICET).

References

[1] Tripathy SC. Simulation of flywheel energy storage system for city buses. Energy Convers Manage 1992;33(4):243–50.
[2] Zhao Y, Lipo T. Space vector pwm control of dual three-phase induction machine using vector space decomposition. IEEE Trans Ind Appl 1995;31(5):1100–9.
[3] Levi E. Multiphase electric machines for variable-speed applications. IEEE Trans Ind Electron 2008;55(5):1893–909.
[4] Suzuki Y, Koyanagi A, Kobayashi M, Shimada R. Novel applications of the flywheel energy storage system. Energy 2005;30(11):2128–43.
[5] Tzeng J, Emerson R, Moy P. Composite flywheels for energy storage. Compos Sci Technol 2006;66(14):2520–7.
[6] Liu H, Jiang J. Flywheel energy storage-an upswing technology for energy sustainability. Energy Build 2007;39(5):599–604.
[7] Kondoh J, Ishii I, Yamaguchi H, Murata A, Otani K, Sakuta K, et al. Electrical energy storage systems for energy networks. Energy Convers Manage 2000;41(17):1863–74.
[8] Koshizuka N, Ishikawa F, Nasu H, Murakami M, Matsunaga K, Saito S, et al. Progress of superconducting bearing technologies for flywheel energy storage systems. Phys C: Supercond 2003;386(11):444–50.
[9] Holmes TA, Lipo DG. Pulse width modulation for power converters: principles and practice. John Wiley; 2003.
[10] Bornemann H, Sander M. Conceptual system design of a 5 mwh/100 mw superconductive flywheel energy storage plant for power utility applications. IJBC 1997;7(2):398–401.
[11] Aanstoos TA, Kajs JP, Brinkman WG, Liu HP, Ouroua A, Hayes RJ, et al. High voltage stator for a flywheel energy storage system. IEEE Trans Magn 2001;37(1):242–7.
[12] Bose BK, Kim MH, Kankam MD. Power and energy storage devices for next generation hybrid electric vehicle. In: Proc. of the 31st intersociety - energy conversion engineering conf., vol. 39; 1996. p. 1893–8.
[13] Kenny B, Kascak P, Jansen R, Dever T, Santiago W. Control of a high-speed flywheel system for energy storage in space applications. IEEE Trans Ind Appl 2005;41(4):1029–38.
[14] Tsao P, Senesky M, Sanders S. An integrated flywheel energy storage system with homopolar inductor motor/generator and high frequency drive. IEEE Trans Ind Appl 2003;39(6):1710–25.
[15] Bernard N, Ahmed HB, Multon B. Axial-field synchronous machine with homopolar flux in the airgap for a flywheel accumulator. IEEE Trans Magn 2002;27(6):1258–65.
[16] Alan I, Lipo T. Induction machine based flywheel energy storage system. IEEE Trans Aerospace Electron Syst 2003;39(1):151–63.
[17] Boglietti A, Ferrari P, Lazzari M, Profumo F. Iron losses in magnetic materials with six-step and pwm inverter supply. IEEE Trans Magn 1991;27(6):242–7.
[18] Senesky M, Tsao P, Sanders S. Simplified modelling and control of a synchronous machine with variable-speed six-step drive. APEC'04 2004;3:1803–9.
[19] Amodeo S, Leon A, Chiacchiarini H, Solsona J, Busada C. Nonlinear control strategies of a flywheel driven by a synchronous homopolar machine. IEEE Int Symp Ind Electron 2007:227–32.
[20] Isidori A. Nonlinear control systems. An introduction. 3rd ed. London, Great Britain: Springer-Verlag; 1995.
[21] Bodson M, Chiasson J, Novotnak R. High-performance induction motor control via input–output linearization. IEEE Control Syst Mag 1994;14:25–33.
[22] Ilic'-Spong M, Marino R, Peresada S, Taylor D. Feedback linearizing control of switched reluctance motors. IEEE Trans Autom Control 1987;32:371–9.
[23] Solsona J, Valla M, Muravchik C. A nonlinear reduced order observer for permanent magnet synchronous motors. IEEE Trans Ind Electron 1996;43(4):492–7.